

**Shining Light on Dark Matter,
One Photon at a Time**

by

Brandon Leigh Allen

Submitted to the Department of Physics
in partial fulfillment of the requirements for the degree of

Doctorate of Science in Physics

at the

MASSACHUSETTS INSTITUTE OF TECHNOLOGY

June 2019

© Massachusetts Institute of Technology 2019. All rights reserved.

Author
Department of Physics
May 18, 2019

Certified by
Christoph E.M. Paus
Professor
Thesis Supervisor

Accepted by
Nergis Mavalvala
Associate Department Head for Education

**Shining Light on Dark Matter,
One Photon at a Time**

by

Brandon Leigh Allen

Submitted to the Department of Physics
on May 18, 2019, in partial fulfillment of the
requirements for the degree of
Doctorate of Science in Physics

Abstract

A search is conducted for new physics in final states containing a photon and missing transverse momentum in proton-proton collisions at $\sqrt{s} = 13$ TeV. The data collected by the CMS experiment at the CERN LHC correspond to an integrated luminosity of 35.9 inverse femtobarns. No deviations from the predictions of the standard model are observed. The results are interpreted in the context of dark matter production and limits on new physics parameters are calculated at 95% confidence level. For the two simplified dark matter production models considered, the observed (expected) lower limits on the mediator masses are both 950 (1150) GeV for 1 GeV dark matter mass.

Thesis Supervisor: Christoph E.M. Paus

Title: Professor

Acknowledgments

This is the acknowledgements section. You should replace this with your own acknowledgements.

Contents

1	Dark Matter	11
1.1	Astrophysical Evidence	12
1.1.1	Galactic Clusters	12
1.1.2	Galactic Rotation Curves	13
1.1.3	Gravitational Lensing	14
1.1.4	Cluster Collisions	15
1.2	Relic Density	18
1.3	Dark Matter Candidates	20
1.3.1	Weakly-Interacting Massive Particles	21
1.3.2	Axions	21
1.3.3	Sterile Neutrinos	22
1.4	Simplified Models for LHC	24
1.5	Non-collider Searches	25
1.5.1	Direct Detection	26
1.5.2	Indirect Detection	29

Chapter 1

Dark Matter

As a theory of the fundamental particles and forces of nature, the Standard Model should also help explain physics at the largest scales. The Λ CDM model best explains all current cosmological observations including the structure of the cosmic microwave background; the abundances of hydrogen, helium, and lithium; the large-scale structure in the distribution of galaxies, and the accelerating expansion of the universe. However, the latest results from the Planck collaboration show that baryonic matter (matter consisting of various combinations of protons, neutrons, and electrons) only contributes $\sim 5\%$ of the total energy of the universe, with radiation (photons and relativistic neutrinos) contributing less than a hundredth of a percent.

The remaining 95% of energy comes from just two sources: $\sim 27\%$ from non-relativistic non-baryonic matter referred to as dark matter and $\sim 68\%$ from an unknown form of energy that permeates all of space referred to as dark energy. Current observations show that dark energy is uniform in space and time producing a similar effect to that of the cosmological constant in the Einstein field equations of general relativity. Not much else is known about dark energy, although there are many experiments attempting to discover additional properties. The work in this thesis shall focus on trying to explain dark matter.

Dark matter cannot be explained by the 17 particles of the Standard Model (see Section 1.3), yet its gravitational effects have been observed in many circumstances. The rest of this chapter will cover the astrophysical evidence for dark matter (Sec-

tions 1.1 and 1.2), various dark matter candidates (Section 1.3), and non-collider searches for dark matter (Section 1.5) before concluding with a discussion of the dark matter models investigated in this thesis (Section 1.4).

1.1 Astrophysical Evidence

All existing evidence for dark matter comes from astrophysical observations of its gravitational effects on the universe at various length scales. We shall focus on four different sources of evidence: the average velocity of galaxies in clusters, the rotation curves of spiral galaxies, strong gravitational lensing, and merging galactic clusters. The evidence presented here is not exhaustive, see Reference ?? for more detail.

1.1.1 Galactic Clusters

Galactic clusters are the largest gravitational bound systems, with the orbital velocities of the individual clusters determined by the total gravitational mass of the cluster. Applying the Virial Theorem gives the explicit relation

$$v^2 = \frac{GM}{2r}, \quad (1.1)$$

where v is the average orbital velocity of a galaxy in the cluster, r is the average separation between galaxies in the cluster, M is the total gravitational mass of the cluster, and G is the Newtonian constant of gravitation. In 1933, Fritz Zwicky measured the average orbital velocity of the Coma cluster and discovered that it was a factor of ten larger than the observed visible mass of the Coma cluster, leading to the conclusion that the majority of the cluster consisted of non-luminous matter. Today studies show that stars only contribute 1% of the total cluster mass, with a hot, baryonic intracluster medium and dark matter contributing the remaining 14% and 85% of the total cluster mass, respectively.

1.1.2 Galactic Rotation Curves

Spiral galaxies are stable gravitational bound systems with stars and interstellar gas rotating around the galactic center in nearly circular orbits in a single plane. For these galaxies, the orbit of an individual star is stable when the gravitational force acting on the star balances the centripetal acceleration of the star. With this condition, the expected stellar velocity v is a function of distance r from the galactic center given by

$$v = \sqrt{\frac{GM(r)}{r}} \quad (1.2)$$

where $M(r)$ is the total gravitational mass inside radius r . Thus, past a certain critical radius r_c , the stellar velocity should fall with as $r^{1/2}$ as the mass of the galaxy is no longer increasing.

In 1980, Vera Rubin and Kent Ford observed that instead of decreasing at distances outside the visible galaxy, the stellar velocity stayed constant out to a very great distance, necessitating an additional non-luminous source of mass. The most common explanation for this missing mass is the existence of an isotropic dark matter halo surrounding the galaxy. With the inclusion of interstellar gas, the total mass inside radius r is given by

$$M(r) = 4\pi \int_0^r dr' (r')^2 [\rho_S(r') + \rho_g(r') + \rho_{DM}(r')], \quad (1.3)$$

where ρ_S , ρ_g , and ρ_{DM} are the density profiles of the stars, interstellar gas, and dark matter in the galaxy, respectively. Once these densities have been specified, it is possible to plot the fraction of the total stellar velocity due to each mass source as a function of distance from the galactic center.

Figure 1-1 shows the results of doing this using the observed stellar and interstellar mass density profiles and the expected density from an isotropic dark matter halo for two different spiral galaxies. In both cases, this reproduces the observed flat galactic rotation curve incredibly well, lending strong support for the existence of galactic dark matter halos.

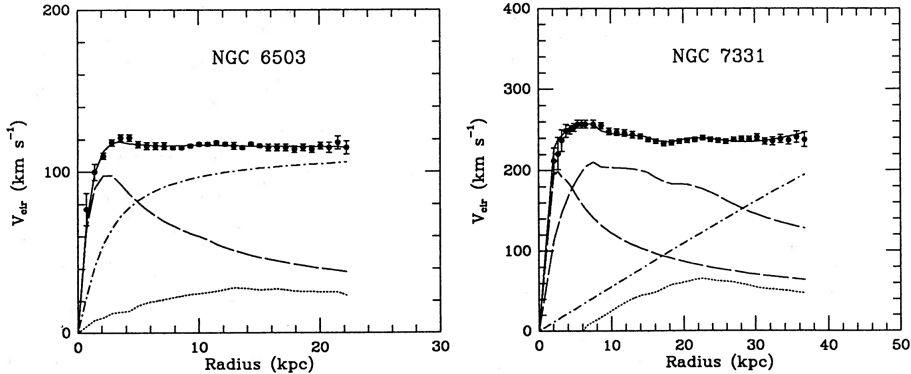


Figure 1-1: The observed (points) and fitted (solid line) rotation curves for two sample galaxies. The fit consists of three components: the stellar component (dashed), the interstellar gas (dotted), and the dark matter halo (dash-dotted). Reprinted from Reference [1].

1.1.3 Gravitational Lensing

As a consequence of Einstein's equivalence principle, a massive body will deflect light, a phenomenon known as gravitational lensing. In the language of general relativity, this means that the photons take the path given by the geodesic lines following the curvature of space-time due to the massive body. For most observations of gravitational lensing due to astrophysical bodies, the physical size of the lensing object is much smaller than the distance between observer, lens, and source allowing us to use the thin lens approximation. Approximating the lens as a planar distribution of matter, the angular deflection is given by

$$\vec{\alpha}(\vec{x}) = \frac{4G}{c^2} \int d^2x' \frac{\vec{x} - \vec{x}'}{|\vec{x} - \vec{x}'|^2} \int dz \rho(\vec{x}', z) \quad (1.4)$$

where \vec{x} is a two-dimensional vector in the plane of the lens, z is the perpendicular distance from the plane of the lens, and ρ is the three dimensional density. If the source is treated as a point mass, this reduces to

$$\alpha = \frac{4G}{c^2} \cdot \frac{M}{b} \quad (1.5)$$

where $b = |\vec{x} - \vec{x}'|$ is the impact parameter and M is the total mass of the object. Thus, measuring the angle of deflection due to gravitational lensing around an astrophysical object provides an independent measurement of the total mass of the body which can be compared against the mass of the luminous objects in the body.

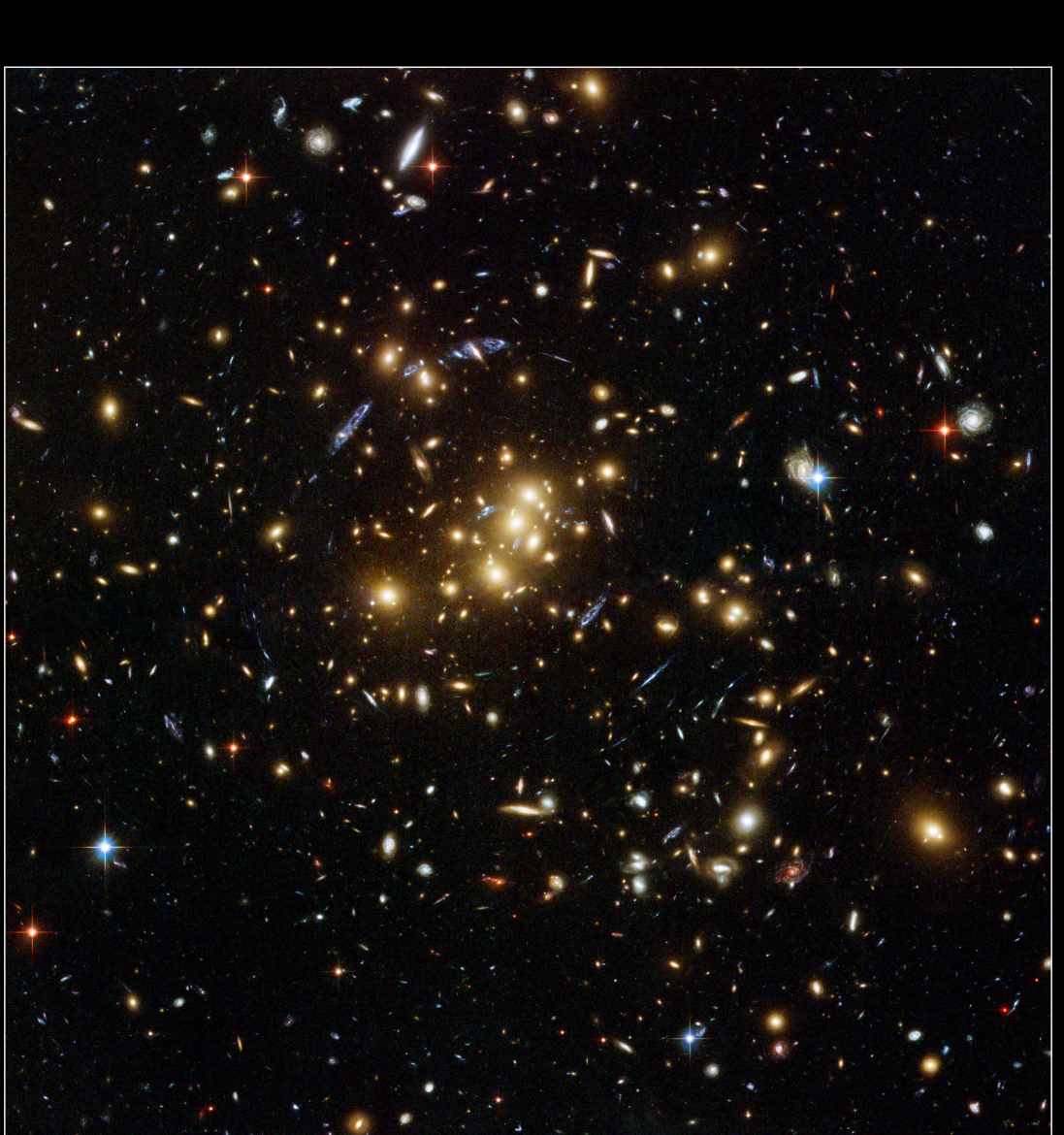
Depending on the mass of the deflecting body and impact parameter, the size of deflection can fall into three different regimes. The first of these is called strong lensing where the curving of space-time is so strong that light can travel multiple paths around the lens and still reach the observer. If the source is directly behind a circular lens, light travels around all sides of the lens and appears as an Einstein ring, while if the source is offset or the lens is non-circular, the source will instead appear in multiple locations as if viewed from slightly different angles. An example of strong lensing is shown in Figure 1-2.

The next regime is known as weak lensing, where the deflection is enough to distort the image of the source but not enough to result in multiple images. The shear of this distortion can be converted into a map of the projected mass distribution. True weak lensing results in circular “*E*-mode” patterns while sources of systematic uncertainty produce both “*E*-mode” and curl-like “*B*-mode” patterns. Thus, requiring a zero “*B*-mode” contribution assures that the measured mass distribution is accurate. Figure 1-3 shows the observed shear of half a million galaxies measured in the Hubble Space Telescope COSMOS survey.

The final regime is the microlensing that occurs when a lens moves relative to a luminous source. As the lens passes in front of the source, it will temporarily increase the apparent luminosity of the source, enabling a mass measurement of the lens. Microlensing results show that rocky exoplanets orbit other stars and that these planets cannot form the bulk of dark matter in the Milky Way.

1.1.4 Cluster Collisions

Additionally, gravitational lensing measurements of galactic cluster collisions provide support for dark matter and help constrain its properties. Figure 1-4 shows the merging cluster 1E0657-558. By comparing the weak lensing reconstruction of



Galaxy Cluster Cl 0024+17 (ZwCl 0024+1652)
Hubble Space Telescope • ACS/WFC

NASA, ESA, and M.J. Jee (Johns Hopkins University)

STScI-PRC07-17b

Figure 1-2: Strong gravitational lensing around galaxy cluster CL0024+17, consisting of the gravitationally bound yellow, elliptical galaxies. The elongated blue objects are from much more distant galaxies behind the cluster which are distorted into arcs due to gravitational lensing from the dark matter halo surrounding the cluster. Figure credit: NASA, ESA, M.J. Jee and H. Ford (Johns Hopkins University)

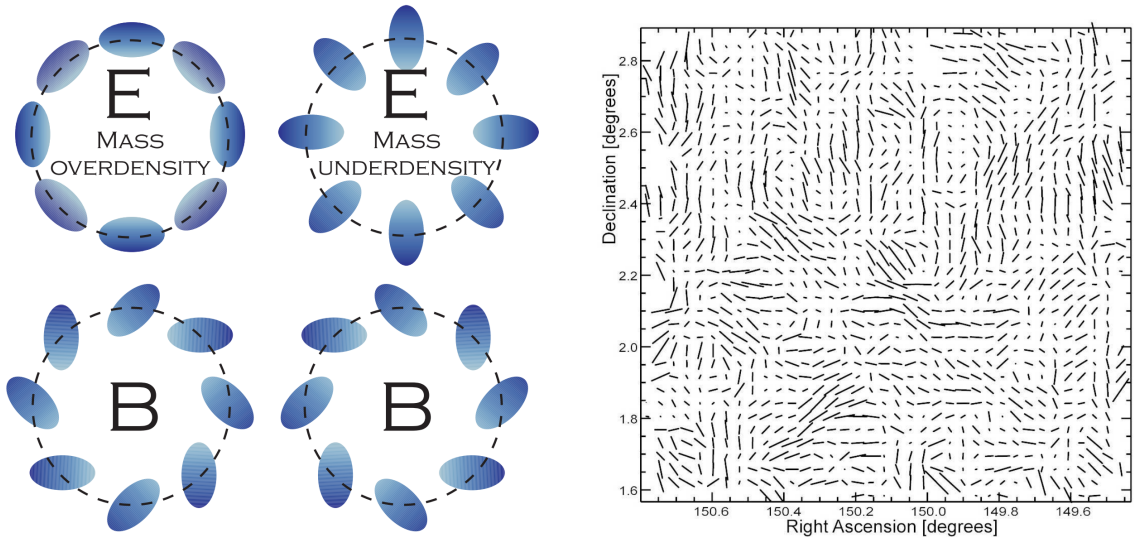


Figure 1-3: Left: Examples of circular “E-mode” and curl-like “B-mode” patterns. Right: The observed ellipticities of half a million distant galaxies within the 2 square degree Hubble Space Telescope COSMOS survey. Reprinted fom Reference [1].

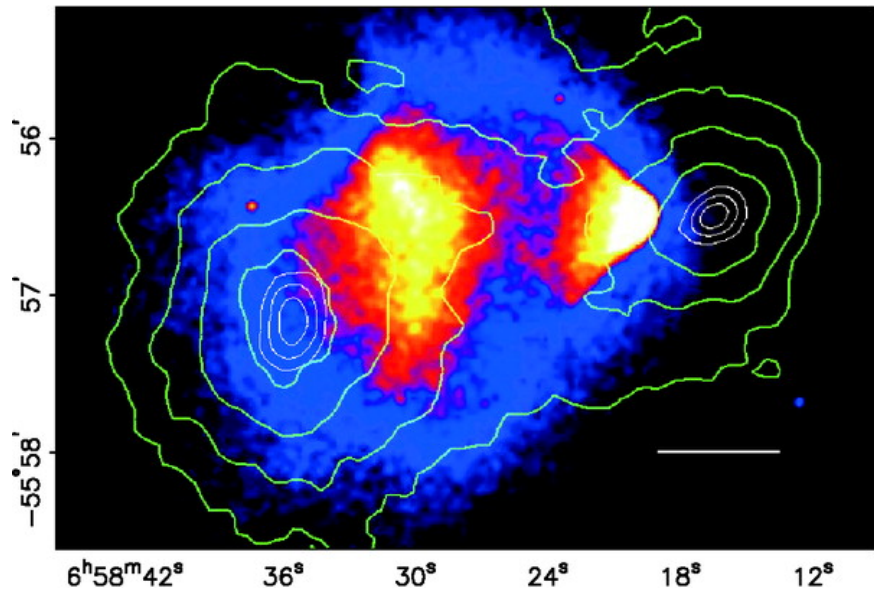


Figure 1-4: The merging cluster 1E0657-558. The green contours show the weak lensing reconstruction of the gravitational potential of the cluster. The colors indicate the X-ray temperature of the plasma, changing from blue to white as the plasma goes from coolest to hottest. The smaller “bullet” cluster on the right which traversed through the larger cluster on the left. Reprinted from Reference [2].

the gravitational potential of the cluster shown in green contours against temperature color gradient of the X-ray emitting interstellar plasma, it was learned that the gravitational potential of the cluster does not track the dominant baryonic mass contribution coming from the plasma. Instead, the gravitational potential tracks the smaller stellar baryonic mass component. Dark matter must be the dominant gravitational source in the cluster since the center of total mass is offset from the center of baryonic mass. Furthermore, the observation of two gravitational mass centers places strong constraints on the self-interaction of dark matter requiring that the observed mass must have a self-interaction collisional cross section $\sigma/m < 1.25 \text{ cm}^2\text{g}^{-1}$ at a 68% confidence level.

1.2 Relic Density

During the early universe, dark matter (DM) was in thermal equilibrium with the rest of the SM particles with a number density n_χ given by

$$n_\chi^{\text{eq}} = \frac{g}{(2\pi)^3} \int f(\vec{p}) d^3\vec{p}, \quad (1.6)$$

where g is the number of internal degrees of freedom of the DM particle χ and $f(\vec{p})$ is either the Fermi-Dirac or Bose-Einstein distribution, depending on the quantum statistics of the DM particle. At very high temperatures relative to the mass m_χ of the DM particle, dark matter and SM particles rapidly convert back and forth with a DM annihilation rate $\Gamma = \langle \sigma_A v \rangle \cdot n_\chi$, where $\langle \sigma_A v \rangle$ is the thermally averaged product of the total cross section for annihilation σ_A and the relative velocity v of the dark matter particles. After the temperature drops below m_χ , the DM annihilation rate Γ drops below the Hubble expansion rate H of the universe and the DM particles stop annihilating and freeze-out of equilibrium with the SM particles, leaving the DM relic density that we observe today. During the freeze-out process, the time dependence

of the number density n_χ is described by the Boltzmann equation as follows

$$\frac{dn_\chi}{dt} + 3Hn_\chi = -\langle\sigma_A v\rangle [(n_\chi)^2 - (n_\chi^{\text{eq}})^2]. \quad (1.7)$$

The LHS term accounts for the reduction in density due to the expansion of the universe. The two RHS terms account for the change in density due to annihilation and product of DM particles to and from SM particles, respectively.

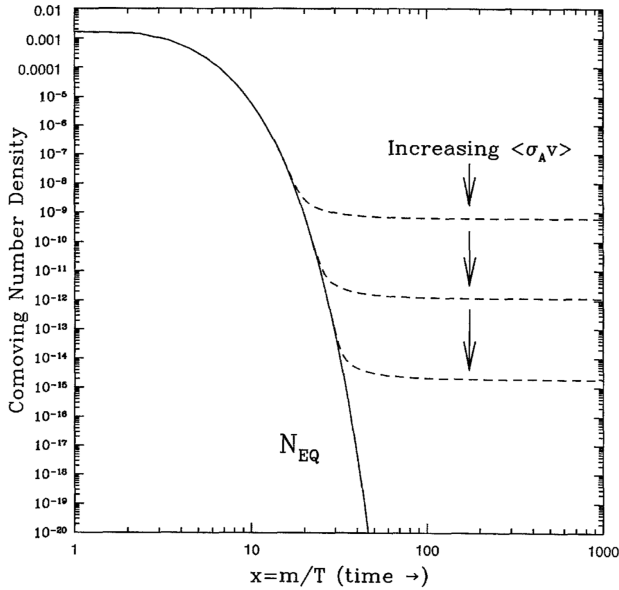


Figure 1-5: Number density of dark matter in the early universe as a function of time. The solid curves are the equilibrium abundance while the dashed curves are the actual abundance after freeze-out. Reprinted from Reference [1].

Figure 1-5 shows the calculated DM number density n_χ as a function of time in the early universe. As the annihilation cross section increases, the relic density decreases as the dark matter particles stay in equilibrium longer. We shall make an order-of-magnitude estimate of the relic density by assuming that $\langle\sigma_A v\rangle$ is independent of energy. Freeze-out occurs at the temperature T_f where the expansion rate $H(T)$ equals the annihilation rate $\Gamma(T)$. The temperature dependence of Γ is simply that of n_χ , e.g. $\Gamma \propto T^3$. Meanwhile, the early universe is radiation dominated, so we have that $H \propto T^2$. Furthermore, astrophysical measurements (see Section 1.1) can't give direct bounds on the number density, only on the mass density $\rho_\chi = m_\chi n_\chi$.

Additionally, mass densities are usually expressed as a fraction of the critical density of the universe $\rho_c = 3H^2/(8\pi G)$. Combining all of this, the relic density of dark matter is given by

$$\Omega_\chi \cdot h^2 = \frac{m_\chi n_\chi}{\rho_c} \simeq \frac{10^{-27} \text{ cm}^3 \text{ s}^{-1}}{\langle \sigma_A v \rangle}, \quad (1.8)$$

where $h = H_0/(100 \text{ km s}^{-1} \text{ Mpc}^{-1})$ is the reduced Hubble constant. Thus, to first order the DM relic density depends only on two things: the total DM annihilation cross section σ_A and the mass m_χ of the DM candidate, as after freeze-out $T \ll m_\chi$ and the velocity v is strictly proportional to m_χ . The latest Planck results measure that $\Omega_\chi \cdot h^2 = 0.1200 \pm 0.0012$, providing strong constraints on the possible values of σ_A and m_χ .

1.3 Dark Matter Candidates

Any dark matter candidate must satisfy the following criteria:

- No or extremely weak interactions with photons, e.g. be **dark**
- Weak baryonic interactions to preserve the DM halos discussed in Section 1.1.2
- Weak self-interactions as discussed in Section 1.1.4
- The observed relic density discussed in Section 1.2.

These four criteria place stringent requirements on dark matter candidates. The light neutrinos, the only SM particles satisfying the first three conditions, are excluded as the total neutrino relic density has a bound of $\Omega_\nu \cdot h^2 \leq 0.00067$ at 95% confidence level from analysis of the CMB anisotropies. Big Bang Nucleosynthesis and gravitational microlensing have mostly exclude non-luminous baryonic matter from forming the bulk of dark matter. Thus, most theories of dark matter propose a new fundamental particle as a dark matter candidate. The following sections discuss the most common dark matter candidates, namely weakly-interacting massive particles (WIMPs), axions, and sterile neutrinos.

1.3.1 Weakly-Interacting Massive Particles

The annihilation cross-section of new particle χ with electroweak scale interactions is approximately

$$\langle \sigma_A v \rangle \approx \left(\frac{\alpha \cdot g_\chi^2}{m_\chi} \right)^2 = \left(\frac{e^2}{4\pi} \cdot \frac{(0.8)^2}{100 \text{ GeV}} \right)^2 \simeq 10^{-26} \text{ cm}^3 \text{ s}^{-1}, \quad (1.9)$$

where $\alpha = e^2/4\pi$ is the fine-structure constant, $m_\chi = 100 \text{ GeV}$ is the mass of the particle, and $g_\chi \approx 0.8$ is the effective coupling for the four-point interaction $\chi\bar{\chi} \rightarrow f\bar{f}$. Plugging this into Equation 1.8, we obtain $\Omega_\chi \cdot h^2 \sim 0.1$, which is very close to the observed value. This numerical coincidence motivates a new weakly-interacting massive particle (WIMP) as a good DM candidate.

The only criteria to be a WIMP beyond the generic definition of dark matter is that the mass and interaction strength of the new particle must be approximately that of the EWK scale. Thus, a great many new physics models have WIMPS natively, such as the neutralino in supersymmetry and the lightest Kaluza-Klein particle in theories of universal extra dimensions. In this thesis, we shall focus on a set of simplified models that describe WIMP interactions in a relatively model-independent manner. For more details, see Section 1.4.

1.3.2 Axions

The hypothetical axion particle introduced in Section ?? is a dark matter candidate if the axion decay constant f_a is large enough as all axion-SM couplings are inversely proportional to it. Constraints from the observed duration of the neutrino burst from supernova SN 1987A require that $f_a \gtrsim 10^9 \text{ GeV}$, sufficiently high that the axion lifetime exceeds the age of the universe by many orders of magnitude. Thus, the axion is a viable DM candidate due to its long lifetime and weak couplings to SM particles.

After accounting for kinematic mixing with the π^0 and η mesons, the axion mass is given by

$$m_a = \left(\frac{\sqrt{m_u m_d}}{m_u + m_d} \right) \left(\frac{f_\pi}{f_a} \right) m_\pi \simeq \left(\frac{10^7 \text{ GeV}}{f_a} \right) \text{ eV}, \quad (1.10)$$

where f_π is the pion decay constant and m_u , m_d , and m_π are the masses of the up quark, the down quark, and the neutral pion, respectively. From this, we see that the axion mass is inversely proportional to f_a , leading to an upper limit of $m_a \lesssim 10 \text{ meV}$. The Planck measurements of the cosmic microwave background also provide a lower (upper) bound on the axion mass $m_a \gtrsim 10 \mu\text{eV}$ (axion decay constant $f_a \lesssim 10^{12} \text{ GeV}$), otherwise the axion abundance is too high.

The axion obtains a two-photon vertex through loops involving virtual quarks and gluons of the form

$$\mathcal{L}_{a\gamma\gamma} = \frac{1}{4} g_{a\gamma\gamma} \epsilon_{\mu\nu\rho\sigma} F^{\mu\nu} F^{\rho\sigma} a = -g_{a\gamma\gamma} (\vec{E} \cdot \vec{B}) a, \quad (1.11)$$

where $F^{\mu\nu}$ is the electromagnetic field-strength tensor, \vec{E} and \vec{B} are the electric and magnetic fields, respectively, and the coupling constant is

$$g_{a\gamma\gamma} = -\frac{\alpha}{3\pi f_a} \left(\frac{m_u + 4m_d}{m_u + m_d} \right). \quad (1.12)$$

From this, we can see that the axion's coupling to the photon is incredibly small unless in the presence of a strong electromagnetic field. Thus, astrophysical axions are ***dark*** unless they enter a region with such a field. Searches for axions such as CAST[] and ADMX[] exploit this to try to observe axion-to-photon conversions.

1.3.3 Sterile Neutrinos

In Section ??, we introduced mass for the SM fermions through the Higgs mechanism in order to preserve $SU(2)_L$ gauge invariance. However, since the right-handed neutrinos are singlets under the full $SU(3)_C \times SU(2)_L \times U(1)_Y$ gauge of the SM, it is possible to add explicit Majorana mass terms in addition to the Dirac mass terms in

the SM Lagrangian as follows

$$\begin{aligned}
\mathcal{L}_{\nu_R} &= i\bar{\nu}_R \not{\partial} \nu_R - (\bar{\ell}_L Y_\nu \phi_c \nu_R + \bar{\nu}_R Y_\nu^\dagger \phi_c^\dagger \ell_L) - \frac{1}{2} \left(\bar{\nu}_R^c M_M \nu_R + \bar{\nu}_R M_M^\dagger \nu_R^c \right) \\
&= i\bar{\nu}_R \not{\partial} \nu_R - (\bar{\nu}_L M_\nu \nu_R + \bar{\nu}_R M_\nu^\dagger \nu_L) - \frac{1}{2} \left(\bar{\nu}_R^c M_M \nu_R + \bar{\nu}_R M_M^\dagger \nu_R^c \right) \\
&= i\bar{\nu}_R \not{\partial} \nu_R - \frac{1}{2} \left[\begin{pmatrix} \bar{\nu}_L & \bar{\nu}_R^c \end{pmatrix} \begin{pmatrix} 0 & M_\nu \\ M_\nu^T & M_M \end{pmatrix} \begin{pmatrix} \nu_L^c \\ \nu_R \end{pmatrix} + h.c. \right], \tag{1.13}
\end{aligned}$$

where ν_R^c are the charge conjugates of the right-handed neutrinos, $h.c.$ stands for hermitian conjugate, and Y_ν , M_ν , and M_M are the Yukawa, Dirac mass, and Majorana mass matrices for the neutrinos, respectively.

In the limit $M_M \gg M_\nu$, the combined mass matrix has two distinct sets of eigenvalues: the sterile neutrinos ν_s with masses $m_s \simeq M_M$ and the active neutrinos ν_a with masses $m_a \simeq M_\nu^2/M_M$. The active and sterile neutrinos are related to the left- and right-handed neutrinos by the active-sterile mixing matrix $\theta = M_\nu M_M^{-1}$ as follows

$$\begin{aligned}
|\nu_a\rangle &= \cos \theta |\nu_L\rangle + \sin \theta |\nu_R\rangle \\
|\nu_s\rangle &= -\sin \theta |\nu_L\rangle + \cos \theta |\nu_R\rangle. \tag{1.14}
\end{aligned}$$

In this formulation, the active neutrinos are the observed neutrinos of the SM while the sterile neutrino states are a promising dark matter candidate as they only interact with the SM through neutrino oscillations. Furthermore, the sterile neutrinos must have $m_s \simeq$ keV or else they cannot account for the observed masses of DM-dominated objects without violating the Pauli exclusion principle. Fortunately, this constraint also means that the oscillation rate into active neutrinos is low enough that the sterile neutrino lifetime is longer than the age of the universe. Additionally, the Majorana mass term allows for additional CP-violating phases beyond the Dirac phases discussed in Section ???. Astrophysical detection, accelerator production, and neutrinoless double β decay experiments all place constraints on sterile neutrino properties.

1.4 Simplified Models for LHC

Without loss of generality, we assume that dark matter consists of a single Dirac fermion WIMP species χ with mass m_{DM} . In order to observe DM at a hadron collider, there must exist a new mediator particle with mass M_{med} that couples to both SM quarks and χ with couplings g_q and g_{DM} , respectively. In general, this mediator can have any spin structure; for purposes of simplicity, we limit ourselves to the observed mediators in the SM: a spin-0 scalar S , a spin-0 pseudoscalar P , a spin-1 vector V_μ , and a spin-1 axial-vector A_μ (not to be confused with SM photon).

The Lagrangians for these possible mediators are

$$\mathcal{L}_S = \frac{1}{2}M_{\text{med}}^2 S^2 + g_{\text{DM}} \bar{\chi} S \chi + g_q \sum_q \bar{q} Y_q S q \quad (1.15)$$

$$\mathcal{L}_P = \frac{1}{2}M_{\text{med}}^2 P^2 + g_{\text{DM}} \bar{\chi} \gamma^5 P \chi + i g_q \sum_q \bar{q} Y_q \gamma^5 P q \quad (1.16)$$

$$\mathcal{L}_V = \frac{1}{2}M_{\text{med}}^2 V_\mu V^\mu + g_{\text{DM}} \bar{\chi} \not{V} \chi + g_q \sum_q \bar{q} \not{V} q \quad (1.17)$$

$$\mathcal{L}_A = \frac{1}{2}M_{\text{med}}^2 A_\mu A^\mu + g_{\text{DM}} \bar{\chi} \gamma^5 \not{A} \chi + g_q \sum_q \bar{q} \gamma^5 \not{A} q, \quad (1.18)$$

where $\{q\}$ and $\{Y_q\}$ are the SM quarks and their associated Yukawa couplings and we have assumed that the coupling g_q is universal to all quarks without any loss of generality. The width of the mediators is determined by the coupling constants and mass of the mediator. Thus, these four models are described by only four parameters in addition to the spin structure of their couplings: $\{g_q, g_{\text{DM}}, m_{\text{DM}}, M_{\text{med}}\}$.

As the CMS detector is focused on observing particles through electromagnetic and strong interactions (see Chapter ??), the production of DM particles alone does not result in an observable signature in the detector. Instead, we look for events where they are produced in association with a visible SM particle with the resulting signature of the SM particle recoiling against an invisible state. The standard mechanism for producing this final state is for one of the incoming partons to radiate the visible SM particle, usually a quark or a gauge boson. The possible final states split into the

categories shown in Table 1.1 with unique final states and interaction strengths.

Table 1.1: Final states of DM production with approximate interaction strength.

Name	Strength	Final State
Monojet	$\mathcal{O}(\alpha_s)$	$j + \chi\bar{\chi}$
Monophoton	$\mathcal{O}(\alpha)$	$\gamma + \chi\bar{\chi}$
Mono- Z	$\mathcal{O}(\alpha)/M_Z^2$	$\ell\ell + \chi\bar{\chi}$

The monojet final state has the highest production rate but also the largest amount of background from SM processes. The Mono- Z final state is the cleanest signature but also a substantially suppressed production rate due to the mass of the Z boson and the small branching ratio to leptons. The monophoton final state lands in the middle on both metrics: the production rate is $\sim 1/10$ that of the monojet final state but also has fewer backgrounds from SM processes. Additionally, the monophoton state has the “advantage” of being able to distinguish between the spin-0 and spin-1 mediators by virtue of the $gg \rightarrow \gamma S$ and $gg \rightarrow \gamma P$ processes being forbidden by Furry’s theorem. For the bulk of this thesis, we focus on the monophoton final state, saving comparisons against the monojet and mono- Z states for Chapter ??.

1.5 Non-collider Searches

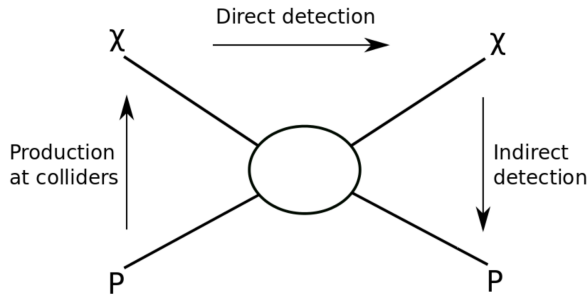


Figure 1-6: Possible dark matter detection channels. Reprinted from Reference [].

The goal of a collider-based search for dark matter is to create pairs of DM candidates through quark-antiquark annihilation, i.e. $q\bar{q} \rightarrow \chi\bar{\chi}$. However, there are other ways you can look at this interaction to attempt to find dark matter, as shown in

Figure 1-6. The longest running searches for DM particles have been direct detection searches, where one attempts to observe the scattering of a DM particle off of a heavy nucleus, i.e. $q\chi \rightarrow q\chi$. Yet another method involves the inverse process utilized at hadron colliders, the observation of SM particles produced in the annihilation of astrophysical DM pairs, i.e. $\chi\bar{\chi} \rightarrow q\bar{q}$. In this section, we shall give a brief overview of the leading experiments for these two approaches.

1.5.1 Direct Detection

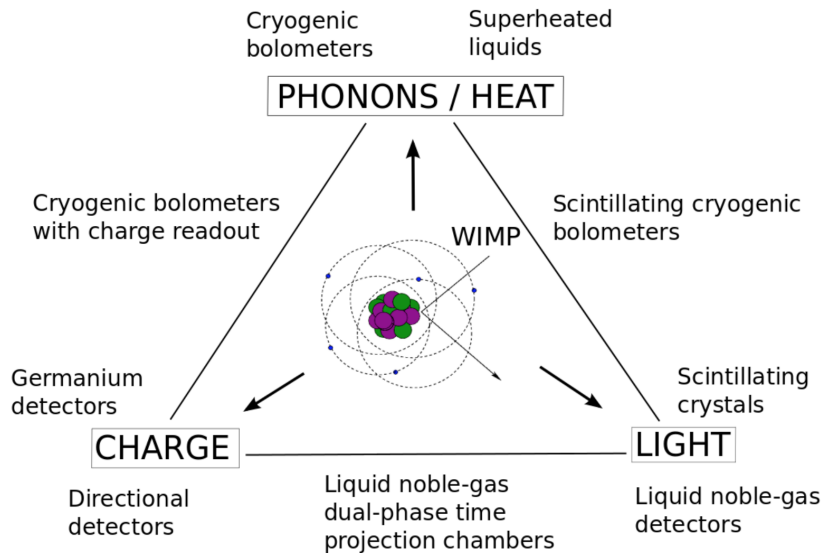


Figure 1-7: Possible signals measured and technologies used in direct detection experiments. Reprinted from Reference [1].

Direct detection experiments aim to observe a collision between a DM particle χ and an atomic nucleus N . The typical nuclear recoil for such a collision is in the $1 - 100 \text{ keV}$ range and there are various different technologies that are used to identify the recoiling nucleus, as shown in Figure 1-7. The three main signals are light from a scintillating material, charge from an ionization reaction, and the product of heat and/or phonons. Many detectors utilize multiple signals in order to enhance background rejection. A final consideration is whether the interaction is spin-independent (SI) or spin-dependent (SD), corresponding to a vector or axial

mediator, respectively. The SI DM-nucleus cross-section scales as the number of nucleons squared and thus experiments focusing on SI interactions use materials with a large atomic number. Conversely, the spin-dependent DM-nucleus cross-section depends on the total nuclear spin and experiments focusing on SD interactions use materials with an odd number of nucleons, particularly those with unpaired protons and neutrons. The remainder of this section will discuss three proto-typical direct detection experiments.

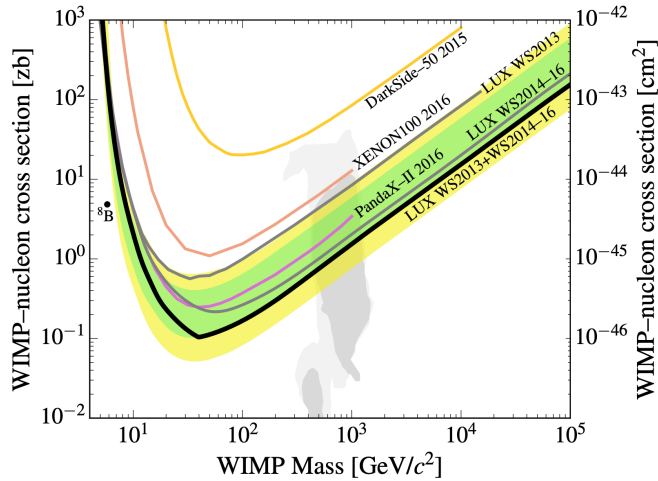


Figure 1-8: Latest SI independent results from the LUX experiment (brazilian flag bands). Reprinted from Reference [1].

The Large Underground Xenon (LUX) experiment is a dual-phase xenon time projection chamber that utilizes both scintillation light and free electrons from ionization to detect nuclear recoils. The active detector volume has 250 kg of ultrapure liquid xenon, a large enough volume that the detector is self-shielding. Odd isotopes make up 47% of naturally occurring xenon, enabling measurements of spin-dependent interactions with approximately half the active detector volume. The latest LUX results are shown in Figure 1-8.

The CDMSlite experiment uses a cryogenic germanium bolometer that detects phonons and ionization from nuclear recoils. The presence of both signals allows for particle identification, but the most sensitive results only use the phonon signals. CDMSlite is most sensitive to dark matter with masses between 1-10 GeV as shown

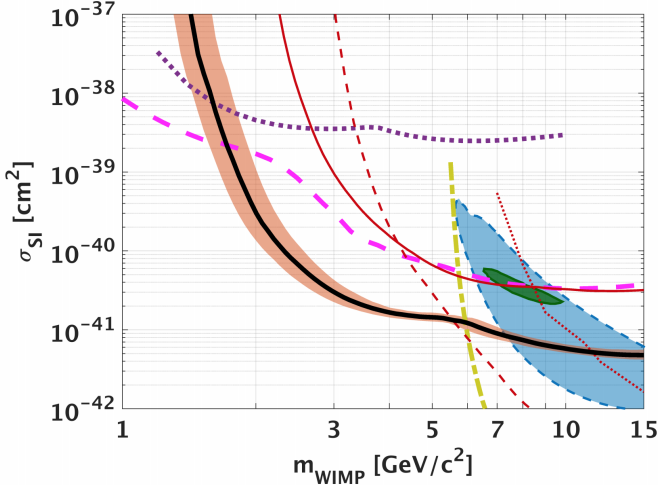


Figure 1-9: Latest SI independent results from the CDMSlite experiment (black line with salmon band). Reprinted from Reference [1].

in Figure 1-9.

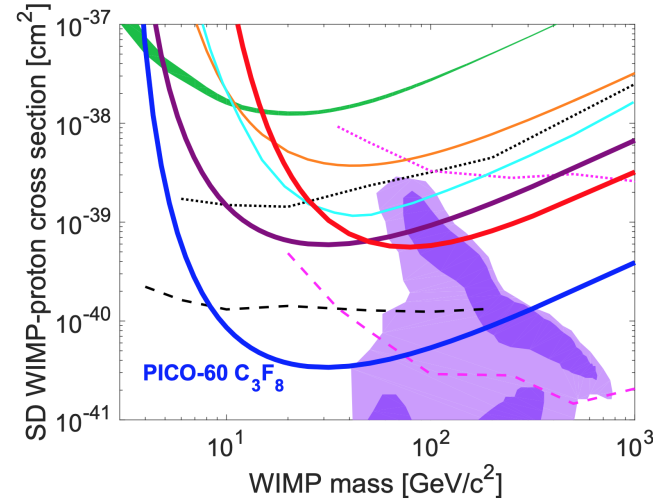


Figure 1-10: Latest SD independent results from the PICO-60 experiment (thick blue line). Reprinted from Reference [1].

The PICO-60 experiment uses a bubble chamber filled with C_3F_8 to observe nuclear recoils with a threshold of 13.6 keV. This threshold is high enough to reject backgrounds from minimum ionizing particles while still having sufficient signal efficiency. Furthermore, fluorine has exactly one unpaired proton and no unpaired neutrons, greatly enhancing the sensitivity to the proton-coupling SD interactions.

The latest results from PICO-60 are shown in Figure 1-10.

1.5.2 Indirect Detection